Research Article Vol. 30, No. 4 / 14 Feb 2022 / Optics Express 5879

Optics EXPRESS

Near-infrared plasmonic sensing and digital metasurface via double Fano resonances

XIAOFENG XU,[1,7] XIAO-QING LUO,[1,2,7,8] JINGZHAO ZHANG,[1] WEIHUA ZHU,[1] ZHIYONG CHEN,[1] TIE-FU LI,[2] W. M. LIU,[3,4,5] AND XIN-LIN WANG[1,6,9]

[1] *Hunan Province Key Laboratory for Ultra-Fast Micro/Nano Technology and Advanced Laser Manufacture, School of Electrical Engineering, University of South China, Hengyang 421001, China*
[2] *Beijing Academy of Quantum Information Sciences, Beijing 100193, China*
[3] *Beijing National Laboratory for Condensed Matter Physics, Institute of Physics, Chinese Academy of Sciences, Beijing 100190, China*
[4] *School of Physical Sciences, University of Chinese Academy of Sciences, Beijing 100190, China*
[5] *Songshan Lake Materials Laboratory, Dongguan, Guangdong 523808, China*
[6] *School of Mechanical Engineering, University of South China, Hengyang 421001, China*
[7] *Equal contributors*
[8] *xqluophys@gmail.com*
[9] *wxl_ly000@aliyun.com*

Abstract: Plasmonic sensing that enables the detection of minute events, when the incident light field interacts with the nanostructure interface, has been widely applied to optical and biological detection. Implementation of the controllable plasmonic double Fano resonances (DFRs) offers a flexible and efficient way for plasmonic sensing. However, plasmonic sensing and digital metasurface induced by tailorable plasmonic DFRs require further study. In this work, we numerically and theoretically investigate the near-infrared plasmonic DFRs for plasmonic sensing and digital metasurface in a hybrid metasurface with concentric ϕ-shaped-hole and circular-ring-aperture unit cells. We show that a plasmonic Fano resonance, resulting from the interaction between a narrow and a wide effective dipolar modes, can be realized in the ϕ-shaped hybrid metasurface. In particular, we demonstrate that the tailoring plasmonic DFRs with distinct mechanisms of actions can be accomplished in three different ϕ-shaped hybrid metasurfaces. Moreover, the resonance mode-broadening and mode-shifting plasmonic sensing can be fulfilled by modulating the polarization orientation and the related geometric parameters of the unit cells in the near-infrared waveband, respectively. In addition, the plasmonic switch with a high ON/OFF ratio can not only be achieved but also be exploited to establish a single-bit digital metasurface, even empower to implement two- and three-bit digital metasurface characterized by the plasmonic DFRs in the telecom L-band. Our results offer a new perspective toward realizing polarization-sensitive optical sensing, passive optical switches, and programmable metasurface devices, which also broaden the landscape of subwavelength nanostructures for biosensors and optical communications.

1. Introduction

It is known that surface plasmons are collective electron density oscillations when light couples with the conduction electrons on a metal/dielectric interface, which could induce prominent electromagnetic field enhancement. The surface plasmon resonance that can exhibit propagated or localized properties depends on the size and geometry of the structure, which has a wide range of applications, such as biosensing [1–4], infrared remote sensing [5,6] and optical waveguide [7], etc. The plasmonic metasurfaces that are ultrathin two-dimensional structures offer the advantages of the ability to control light with arranged nano/micro-structures patterned on their

#452134 https://doi.org/10.1364/OE.452134
Journal © 2022 Received 22 Dec 2021; revised 22 Jan 2022; accepted 27 Jan 2022; published 8 Feb 2022

surfaces, which can be readily fabricated in both the microwave and optical regimes [8–10]. The optical metasurfaces, which compose of periodic subwavelength unit cells arranged in a specific order, can be applied for integrated optical devices owing to their artificial freedom in design and device miniaturization. These optical metasurfaces indeed offer a universal platform for flexible control of the amplitude, phase, and polarization of the incident light, which imply greater functionality. Heretofore, there have been a dramatic increase in the study of metalens [11,12], beam splitters [13,14], imaging spectrometers [15], optical filters [16], optical switching [17], and so on, in optical metasurfaces.

Fano resonance (FR) first theoretically explained by Ugo Fano is characterized by a sharp and asymmetric lineshape in the absorption profile of noble gas. This behavior is due to the interference between a discrete state and a broad continuum of state, which have been adopted to elucidate plenty of phenomena in various systems [18–21]. Recently, it has been shown that plasmonic systems have proven to be the most active platforms for realizing FR and its applications, since they are more suited for generating the coherent coupling effects [22–25]. Therein, a broad resonance mode plays the role of the continuum state, while a narrow resonance mode can be treated as a discrete state. Based on a spectrum overlapping in the transmittance or reflection spectrum, the plasmonic FR typically occurs via the destructive interference between subradiative (discrete state) and superradiative (continuum state) modes, forming hybridized bonding and anti-bonding modes in metallic metasurfaces [26]. Moreover, compared with a single FR, plasmonic DFRs that are more sensitive to the conformational variation of nanostructures have garnered ever-increasing attention, such as optical filters [16], three-dimensional plasmon ruler [27], slow light devices [28], and plasmonic sensing [29,30]. Furthermore, plasmonic DFRs have been observed in asymmetrically split rings [31], all-dielectric oligomers [32–34], and metallic cluster chain [35,36], etc. In plasmonic multiparticle systems, a single FR grows out of the collective resonances of multiple particles, with the modulation intensity and range of resonance modes being limited. Whilst the plasmonic DFRs mostly appear in complex and multilayer structures, with few of them supporting flexible amplitude modulation and multi-wavelength information transfer and processing. The difficulties in the fabrication of multiparticle systems further impede the realization of plasmonic DFRs and their practical applications. Therefore, designing a simple and tailorable DFRs system to effectively tune the resonance modes, perform the same function at different wavelengths, as well as switch between functionalities at a specific working wavelength are of great significance in the application of optical metasurfaces. Additionally, the resonance mode-broadening has been proved to be particularly suitable for detecting lossy nanoparticle, and monitoring the change of resonance mode linewidth holds great potential in optical biosensing [1,37]. The mode-shifting sensing, however, can be devoted to detecting changes in physical parameters (such as heat, pressure and magnetic fields) surrounding the whisper gallery mode (WGM) resonators [38]. Also, it has been demonstrated that the polarization-sensitive digital metasurface is capable of yielding potential applications for metallic nanostructures in optical communication [39] and information processing [40]. For the sake of preferably exhibiting the plasmonic sensing and digital metasurface induced by the plasmonic DFRs, more investigations are still quite needed.

In this paper, we numerically and theoretically study the near-infrared plasmonic DFRs for the realization of plasmonic sensing and digital metasurface in a novel hybrid metasurface that consists of periodic Ag film arrays with concentric ϕ-shaped-hole and circular-ring-aperture (CRA) unit cells. The results elucidate that the near-infrared plasmonic FR can be achieved due to the interaction between a narrow and a wide effective dipolar modes, rendering the appearance of double bonding and anti-bonding modes. Interestingly, the plasmonic DFRs can be implemented in reduced-ϕ-shaped, ϕ-shaped, and varied-ϕ-shaped hybrid metasurfaces, respectively, leading to the triple bonding and anti-bonding modes under distinct mechanisms of actions. The simulation results are well verified by both the multimode interference coupled mode theory and plasmon hybridization theory. Subsequently, the resonance mode-broadening plasmonic sensing can be realized by varying the polarization direction of the incident light, whereas the mode-shifting plasmonic sensing can be implemented by modifying the length of ϕ-shaped-hole in the ϕ-shaped hybrid metasurface. In particular, based on the maximal and minimal of the transmittances in the realization of plasmonic sensing, the novel compact dual-wavelength passive plasmonic switches can be realized with the ON/OFF ratios (η) being 18.23 dB and 19.55 dB, respectively. In this scenario, such plasmonic optical switches are beneficial to establish single-bit digital metasurface induced by plasmonic FR, and then can be extended to two- and three-bit digital metasurfaces mainly dominated by the plasmonic DFRs at the telecom L-band. Our results provide the fundamental basis for optical sensing, optical digital processing, modulators, and miniaturized wireless communication systems, and holds great promise for broad applications in all-optical devices.

2. Structure and model

Herein, we propose a hybrid metasurface, which comprises of periodic hole arrays with concentric ϕ-shaped-hole and CRA unit cells, as shown in Fig. 1(a). Quartz is chosen as the substrate with the thickness and the dielectric constant being 225 nm and 2.25 [41], respectively. The silver(Ag) film is adopted to construct nano-hole arrays on the quartz substrate with the thickness being 50 nm [42]. The dielectric constant of Ag film is defined by the improved Drude model due to its low absorption loss in visible and near-infrared wavebands [43]. The incident light field is a modulated ultra-short Gaussian pulse with the central wavelength being 1550 nm, which acts vertically on the substrate and propagates along the positive Y-direction. The surrounding medium is air with the refractive index being 1.0. A zoomed view of the unit cell of the hybrid metasurface in the X–Z plane is presented in Fig. 1(b). P_x and P_z are the periodic length of the

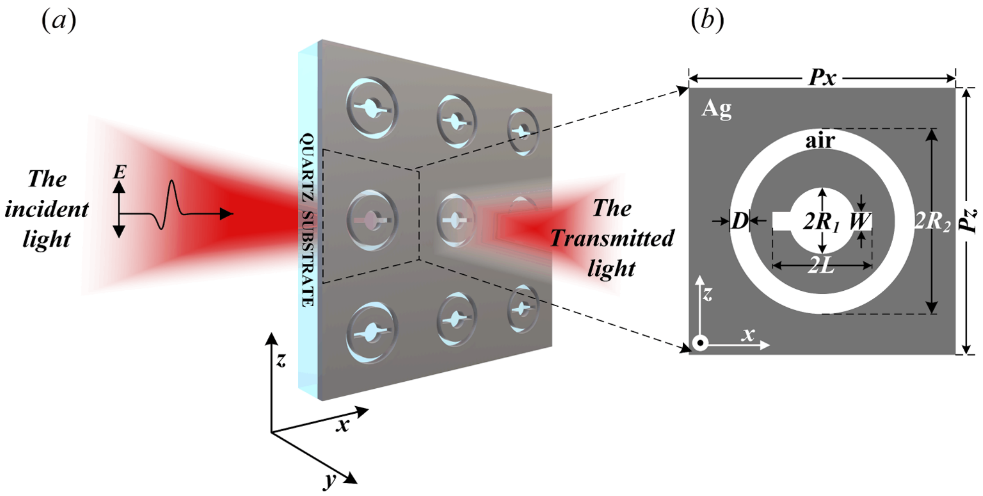

Fig. 1. (a) Schematic diagram of a hybrid metasurface, which consists of periodic silver (Ag) thin-film arrays with concentric ϕ-shaped-hole and circular-ring-aperture unit cells. The linearly polarized incident pulsed light field propagates along the positive Y-direction, which acts vertically on the Ag film from the side of the quartz substrate. (b) Zoomed view of a unit cell of the ϕ-shaped hybrid metasurface in the X-Z plane. The gray and white parts respectively represent the Ag film and the air. R_1 is the radius of the circular-hole with L and W being the length and width of rectangular-hole, respectively, in ϕ-shaped-hole unit cell. D and R_2 are the width and outer radius of the circular-ring-aperture structure, respectively. P_x and P_z are the periodic length of the Ag array in X- and Z-directions, respectively.

periodic hole arrays in X- and Z-directions, respectively. The gray area represents Ag film, while the white area denotes the air. R_1 is the radius of the circular-hole with L and W being the length and width of rectangular-hole, respectively, in the ϕ-shaped-hole unit cell. D and R_2 are the width and outer radius of the CRA unit cell, respectively. The three-dimensional finite-difference time-domain approach is used to analyze the optical transmittance characteristics of the hybrid structure [44,45]. The pulse width is set to 5 fs, and the pulse center time is set as 16 fs. The time step and grid size are set to 5 nm and 8.3 as, respectively, so as to satisfy the needs of the numerical stability conditions. The perfectly matched layers are considered as the boundary conditions on the front and back sides of the Y-direction, which can give rise to a reflectionless absorbing medium that absorbs without any reflected electromagnetic waves at all frequencies and angles of incidence [46,47]. Meanwhile, the X- and Z-direction of the hybrid metasurface are selected as the periodic boundary conditions, which could ensure the continuous distribution of media on the boundary. After the initial value and boundary conditions are given, alternate sampling of electric and magnetic fields is carried out in every half time step, and then iterative calculation is conducted. In order to realize real-time monitoring of the electromagnetic field distribution, a monitoring surface is set at 200 nm above the Ag film.

3. Results and discussions

3.1. Plasmonic Fano resonance in a hybrid metasurface

Here, we study the plasmonic Fano resonance (FR) in a hybrid metasurface that composes of concentrical ϕ-shaped-hole and CRA unit cells (see Fig. 2(c)), compared to two metasurfaces with individual ϕ-shaped-hole (see Fig. 2(a)) and CRA (see Fig. 2(b)) unit cells, respectively. The polarization of the incident light is along the Z-direction. The periods (P_x and P_z) of the unit cells of these metasurfaces all are set as 600 nm. The outer diameter ($2R_2$) and the width (D) of the CRA unit cells are set as 330 nm and 30 nm, respectively. As for the ϕ-shaped-hole of the individual and hybrid metasurfaces, the width (W) and length ($2L$) of the rectangular-hole, as well as the diameter ($2R_1$) of the circular-hole are set to 25 nm, 240 nm, and 110 nm, respectively.

As shown in Fig. 2(a), the transmittance spectrum of the metasurface with individual ϕ-shaped unit cells reveals an asymmetric line shape caused by the interaction between the electric dipole ($\mathfrak{D}_{\phi}^{z}$) and quadrupole ($\mathfrak{Q}_{\phi}^{z}$) modes [48,49]. This process results in the occurrence of pure bonding mode ($\mathfrak{D}_{\phi}^{z} + \mathfrak{Q}_{\phi}^{z}$), which can also be ascertained by the charge distribution of *Ag/air* (top) and *Ag/quartz* (bottom) interfaces in the inset of Fig. 2(a). In the light of the selective excitation that is due to the incident light with specific polarization, this pure bonding mode can be viewed as the effective dipolar mode (D_{ϕ}^{z}), even though the hybridized plasmonic wave functions contain an admixture of $\mathfrak{D}_{\phi}^{z}$ and $\mathfrak{Q}_{\phi}^{z}$ modes [48]. Meanwhile, the transmittance spectrum of the metasurface with individual CRA unit cells depicts the pure bonding mode ($\mathfrak{D}_{\mathrm{CRA}}^{z} + \mathfrak{Q}_{\mathrm{CRA}}^{z}$) that originates from the interaction of electric dipole ($\mathfrak{D}_{\mathrm{CRA}}^{z}$) and quadrupole ($\mathfrak{Q}_{\mathrm{CRA}}^{z}$) modes, which can also be verified by the charge distribution of the related wavelength (yellow dot marking) in the inset of Fig. 2(b). As mentioned above, the bonding mode can also be considered as the effective dipolar mode (D_{CRA}^{z}). It is noteworthy that the linewidth of the effective dipolar mode (D_{ϕ}^{z}) that experiences weak radiation loss is narrower than that of the effective dipolar mode (D_{CRA}^{z}) that is highly radiative [21]. Thus, D_{ϕ}^{z} and D_{CRA}^{z} can be regarded as the subradiant and superradiant modes, respectively [50,51]. As can be seen in Fig. 2(c), the interaction between the superradiant (D_{CRA}^{z}) and subradiant (D_{ϕ}^{z}) modes leads to a pronounced spectral dip in the transmittance spectrum of the hybrid metasurface, indicating the occurrence of plasmonic FR. Based on the plasmon hybridization theory, the plasmonic FR renders the appearance of double bonding ($D_{\phi}^{z} + D_{\mathrm{CRA}}^{z}$) and anti-bonding ($D_{\phi}^{z} - D_{\mathrm{CRA}}^{z}$) modes. This can also be confirmed by the charge distributions (marked with green and purple dots, respectively) in the right side inset of Fig. 2(c).

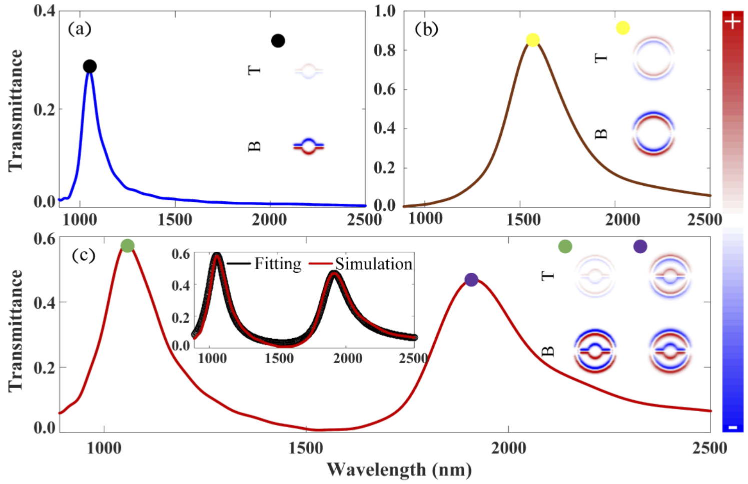

Fig. 2. The near-infrared transmittance spectra of the periodic arrays of (a) individual ϕ-shaped unit cells, (b) individual CRA unit cells, and (c) the hybrid metasurface, respectively. The right side insets show the charge distributions at the labelled wavelength, which represent the top (T) panel at the Ag/air interface and the bottom (B) panel at the Ag/quartz interface, respectively. The insets in (a) and (b) exhibit the charge distribution of individual ϕ-shaped and CRA unit cells at the labelled wavelength, respectively, while the right side inset in (c) shows the charge distribution of the hybrid metasurface. The left side inset in (c) shows the involved transmittance spectrum of the hybrid metasurface, where the red and black solid curves are the simulation and fitting results, respectively. The geometrical parameters of the unit cell of the hybrid metasurface are given as follows: $P_{\rm x}$=$P_{\rm z}$=600 nm, R_1=55 nm, L=120 nm, W=25 nm, D=30 nm, and R_2=165 nm.

To further get insight into the underlying physical mechanism of the plasmonic FR in the ϕ-shaped hybrid metasurface, the multimode interference coupled mode theory (MICMT) can be used to verify our results [52]. It has been deomnstrated that, for multiple resonant modes coupling, the coupling phases of different modes that correlate with each other have a profound impact on their transmittance spectrum. In term of the single mode coupled mode theory, the MICMT fundamental equations with coupling phases can be written as,

$$S_1^{\rm in} = \sum_n S_{n,1}^{\rm in} = \sum_n \gamma_{n1} e^{i\varphi_{n1}} S_1^{\rm in},\ S_2^{\rm in} = \sum_n S_{n,2}^{\rm in} = \sum_n \gamma_{n2} e^{i\varphi_{n2}} S_2^{\rm in}, \tag{1}$$

$$\frac{{\rm d}a_n}{{\rm d}t} = (-\imath\omega - \frac{1}{\tau_{n0}} - \frac{1}{\tau_{n1}} - \frac{1}{\tau_{n2}})a_n + \kappa_{n1} S_1^{\rm in} + \kappa_{n2} S_2^{\rm in}, \tag{2}$$

$$S_1^{\rm out} = -S_1^{\rm in} + \sum_n \kappa_{n1}^{*} a_n,\ \kappa_{n1} = \sqrt{\frac{2}{\tau_{n1}}} e^{i\theta_{n1}}, \tag{3}$$

$$S_2^{\rm out} = -S_2^{\rm in} + \sum_n \kappa_{n2}^{*} a_n,\ \kappa_{n2} = \sqrt{\frac{2}{\tau_{n2}}} e^{i(\theta_{n1} - \phi_n)}, \tag{4}$$

where $S_1^{\rm in(out)}$ and $S_2^{\rm in(out)}$ denote the field amplitudes for the input (output) ports, respectively. γ_{n1} and γ_{n2} are the normalized coefficients which are set as 1 in our scheme. a_n is the field amplitude of the n^{th} resonant mode. ω_n and τ_{n0} are the the resonant frequency and the decay time of internal loss of the n^{th} resonant mode, respectively. τ_{n1} and τ_{n2} represent the decay time of the coupling between the n^{th} resonant mode and the environment, respectively. κ_{n1} and κ_{n2}

depict the coupling coefficients with θ_{n1} and θ_{n2} being the coupling phases (κ_{n1}^* and κ_{n2}^* are the related complex conjugate terms), respectively. ϕ_n is the phase difference between the output and input ports of the n^{th} resonant mode. The MICMT is an effective tool for the study of plasmonic FR phenomena, particularly multiple FRs in the hybrid metasurface. Thus, in case of $S_2^{\text{in}} = 0$, the transmittance of the hybrid metasurface can be given as [53],

$$T = \sum_{n=1}^{N} \frac{2e^{i\varphi_n}}{-i\left(\omega - \omega_n\right)\tau_n + 2 + \frac{\tau_n}{\tau_{n0}}}, \tag{5}$$

with $\varphi_n = \varphi_{n1} + \theta_{n1} - \theta_{n2} + \phi_n$ being the total coupling phase difference for the double bonding ($D_\phi^z + D_{\text{CRA}}^z$) and anti-bonding ($D_\phi^z - D_{\text{CRA}}^z$) modes. By using the MICMT to fit the transmittance spectrum of the hybrid metasurface, the fitting (black solid line) is in a good agreement with the numerical simulation (red solid line) in Fig. 2(c). The fitting parameters of the hybrid metasurface were obtained as follows: $N = 2$, $\omega_1 = 2.8416\times10^{14}$ rad/s, $\omega_2 = 1.5779\times10^{14}$ rad/s, $\tau_1 = 155$ fs, $\tau_2 = 460$ fs, $\tau_{10} = 110$ fs, $\tau_{20} = 195$ fs, $\varphi_1 = 0$, and $\varphi_2 = 0.26$.

3.2. Plasmonic double Fano resonances in three hybrid metasurfaces

In the following, as shown in Fig. 3, we study the controllable near-infrared plasmonic DFRs in three hybrid metasurfaces that consists of reduced ϕ-shaped, ϕ-shaped and varied ϕ-shaped unit cells by adjusting the polarization angle of the incident light field and the width (D) of the CRA unit cells, respectively. Among them, the reduced ϕ-shaped hybrid metasurface (see the right side of the inset in Fig. 3(a)) can be achieved by reducing a rectangle hole of the unit cell in the negative X-direction of the ϕ-shaped hybrid metasurface (see the right side of the inset in Fig. 3(b)), while the varied ϕ-shaped hybrid metasurface (see the right side of the inset in Fig. 3(c)) can be achieved by adding a rectangle hole of the unit cell in the negative Z-direction of the ϕ-shaped hybrid metasurface. From Fig. 3(a), one can see that, with the polarization angle of the incident light being 0°(along the Z-direction), there exists a plasmonic FR in the near-infrared waveband (see the red dashed line). By varying the polarization angle of the incident light to 45°, the depth and width of the plasmonic FR dip obviously decrease (see the black solid line). In this case, the interaction between the double bonding ($D_{\phi_r}^z + D_{\text{CRA}}^z$) and double bonding ($D_{\phi_r}^x + D_{\text{CRA}}^x$) modes leads to the occurrence of the triple bonding mode [($D_{\phi_r}^z + D_{\text{CRA}}^z$)+($D_{\phi_r}^x + D_{\text{CRA}}^x$)], peaked near 1061 nm due to *selective excitation* under specific polarization. It is important to notice that the *degenerate coupling* of double anti-bonding ($D_{\phi_r}^z - D_{\text{CRA}}^z$) and double bonding ($D_{\phi_r}^x + D_{\text{CRA}}^x$) modes, peaked near 1705 nm, solely gives rise to a triple anti-bonding mode [($D_{\phi_r}^z - D_{\text{CRA}}^z$)-($D_{\phi_r}^x + D_{\text{CRA}}^x$)] due to the reduced ϕ-shaped unit cell being excited asymmetrically [54,55]. While the polarization angle of the incident light is changed to 90° (along the X-direction), there is no plasmonic FR on this occasion (see the blue dotted dashed line). These results demonstrate that the strong effective dipolar resonance mode of the reduced ϕ-shaped-hole can be explicitly activated only when the polarization direction of the incident light is perpendicular to the long axis of the rectangular hole, so that the plasmonic FR can be realized [56].

Under the same conditions, as for the ϕ-shaped hybrid metasurface, a similar conclusion can be made when the polarization angle of the incident light is 90° (see the blue dotted dashed line in Fig. 3(b)), but the width of the plasmonic FR dip in the latter case is wider than that of the former case with the polarization angle of the incident light being 0°(see the red dashed line in Fig. 3(b)). Interestingly, as the polarization angle of the incident light is 45°, a new peak appears between the plasmonic FR dip (see the black solid line in Fig. 3(b)), resulting in the realization of plasmonic DFRs. Therein, as previously analyzed with plasmon hybridization theory, the orange dot peaked at 1055 nm (see the black solid line in Fig. 3(b)) only denotes the triple bonding mode [($D_\phi^z + D_{\text{CRA}}^z$)+($D_\phi^x + D_{\text{CRA}}^x$)]. The triple bonding mode, as a result of

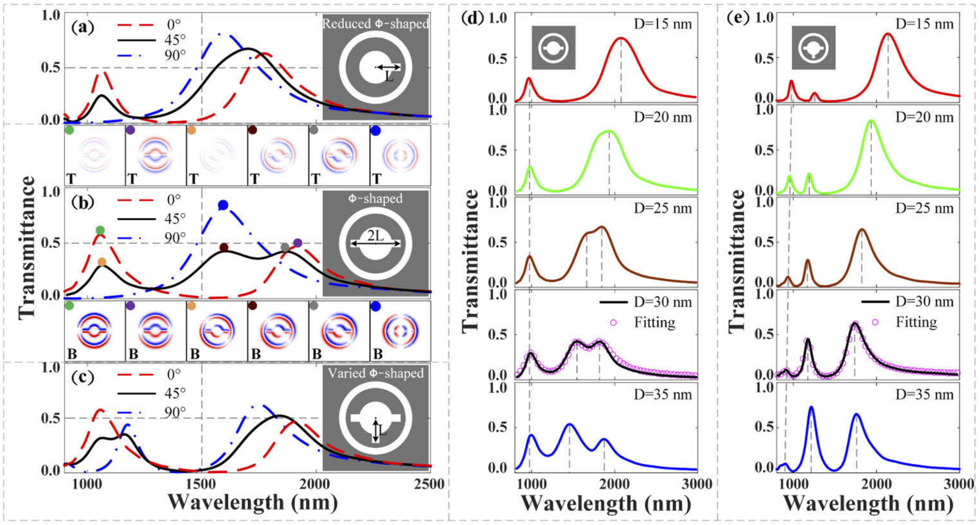

Fig. 3. The tailoring near-infrared plasmonic DFRs in three hybrid metasurfaces. (a-c) Transmittance spectra of the three hybrid metasurfaces with reduced ϕ-shaped, ϕ-shaped and varied ϕ-shaped unit cells, respectively, versus different polarization angles (0°, 45°, and 90°) of the incident light field. The charge distributions of the metasurface with ϕ-shaped unit cells at the labelled wavelength are shown in the insets, which represent the top (T) panel at the Ag/air interface and the bottom (B) panel at the Ag/quartz interface, respectively. (d) The transmittance spectrum for the ϕ-shaped hybrid metasurface with the width (D) of the CRA unit cells varying from 15 to 35 nm, when the polarization angle of the incident light at 45°. (e) The transmittance spectrum for the varied ϕ-shaped hybrid metasurface with the width (D) of the CRA unit cells increasing from 15 to 35 nm, when the polarization angle of the incident light at 90°. The other parameters are the same as Fig. 2.

selective excitation with specific polarization, is formed by the interaction between the double bonding ($D^z_\phi + D^z_{\mathrm{CRA}}$) and double bonding ($D^x_\phi + D^x_{\mathrm{CRA}}$) modes. And the double bonding mode ($D^x_\phi + D^x_{\mathrm{CRA}}$) can be put down to the interaction between two effective dipolar modes (D^x_ϕ and D^x_{CRA}), when the polarization angle of the incident light is 90° (see the blue dotted dashed line). However, the brown and gray dots peaked at 1592 nm and 1864 nm (see the black solid line in Fig. 3(b)) represent the appearance of triple bonding [($D^x_\phi + D^x_{\mathrm{CRA}}$)+($D^z_\phi - D^z_{\mathrm{CRA}}$)] and anti-bonding [($D^x_\phi + D^x_{\mathrm{CRA}}$)-($D^z_\phi - D^z_{\mathrm{CRA}}$)] modes, respectively. The triple bonding and anti-bonding modes are formed by the interaction between the double bonding ($D^x_\phi + D^x_{\mathrm{CRA}}$) and double anti-bonding ($D^z_\phi - D^z_{\mathrm{CRA}}$) modes, which can also be verified from in the charge distributions of the insets in Fig. 3(b).

For the varied ϕ-shaped hybrid metasurface, similar conclusion (see the red dashed line in Fig. 3(c)) can be made with reference to the ϕ-shaped hybrid metasurface, when the polarization angle of the incident light is 0°. In case of the polarization angle of the incident light being 90°, it is of great interest to find that the peaks positioned at 1176 nm and 1746 nm indicate the presence of the double bonding ($D^x_{\phi'} + D^x_{\mathrm{CRA}}$) and anti-bonding ($D^x_{\phi'} - D^x_{\mathrm{CRA}}$) modes (see the blue dotted dashed line in Fig. 3(c)), respectively. This result arises from the interaction between two effective dipolar modes ($D^x_{\phi'}$ and D^x_{CRA}). Surprisingly, as the polarization angle of the incident light is 45°, a new peak occurs between the FR dip peaked at 1160 nm (see the black solid line in Fig. 3(c)), indicating the realization of plasmonic DFRs. In this case, there exists only the occurrence of triple anti-bonding mode [($D^z_{\phi'} - D^z_{\mathrm{CRA}}$)-($D^x_{\phi'} - D^x_{\mathrm{CRA}}$)] near 1835 nm (see the black solid line in Fig. 3(c)), which originates from the *degenerate coupling* between the two double anti-bonding modes. Moreover, the peaks of the transmittance spectrum peaked at 1064 nm and 1160 nm manifest the presence of the triple bonding $[(D^z_{\phi'} + D^z_{\mathrm{CRA}})+(D^x_{\phi'} + D^x_{\mathrm{CRA}})]$ and anti-bonding $[(D^z_{\phi'} + D^z_{\mathrm{CRA}})-(D^x_{\phi'} + D^x_{\mathrm{CRA}})]$ modes, respectively.

Next, we show how the width (D) of the CRA unit cells on the plasmonic DFRs in the ϕ-shaped and varied ϕ-shaped hybrid metasurfaces, respectively. In the ϕ-shaped hybrid metasurface, the polarization angle of the incident light is fixed at 45°. For the relative small width of the CRA unit cells (D = 15 nm), there exists only plasmonic FR dip in the transmittance spectrum (see the red line in Fig. 3(d)), and the *degenerate coupling* of double anti-bonding $(D^z_{\phi} - D^z_{\mathrm{CRA}})$ and double anti-bonding $(D^x_{\phi} + D^x_{\mathrm{CRA}})$ modes occurs near 1705 nm, owing to the ϕ-shaped unit cell being excited asymmetrically. As the width (D) keeps increasing, one can note that both double bonding $(D^z_{\phi} - D^z_{\mathrm{CRA}})$ and double bonding $(D^x_{\phi} + D^x_{\mathrm{CRA}})$ modes shift to smaller wavelength, without showcasing the *degenerate coupling*. When the width (D) increases to 25 nm (see the brown line in Fig. 3(d)), a split appears at the left shoulder of the spectrum (located at 1845 nm), followed by the appearance of a new Fano dip, i.e., plasmonic DFRs. With the increase of the width (D = 30 nm), the width and depth of the new Fano dip become wider and deeper. When the width (D) increases to 35 nm, the width and depth of the new Fano dip get even wider and deeper, resulting in the presence of triple distinct peaks (see the blue line in Fig. 3(d)). With the increase of the width (D), the width and depth of the two Fano dips blueshift, which is mainly attributed to the gradual blueshift of resonant wavelength of the CRA structure. At the same time, the MICMT agrees well with the numerical simulation by using Equation (5), as shown in the pink circles in Fig. 3(d), when the width D equals to 30 nm. The fitting parameters of this plasmonic DFRs can be given as follows: $N = 3$, $\omega_1 = 2.8336 \times 10^{14}$ rad/s, $\omega_2 = 1.8855 \times 10^{14}$ rad/s, $\omega_3 = 1.6006 \times 10^{14}$ rad/s, $\tau_1 = 60$ fs, $\tau_2 = 97$ fs, $\tau_3 = 105$ fs, $\tau_{10} = 285$ fs, $\tau_{20} = 345$ fs, $\tau_{30} = 435$ fs, $\varphi_1 = 0$, $\varphi_2 = 0.0314$, and $\varphi_3 = 0.1571$. For the varied ϕ-shaped hybrid metasurfaces, by fixing the polarization angle of the incident light at 45°, similar conclusions can be obtained, when the width D is changed from 15 nm to 35 nm. When the polarization angle of the incident light is fixed at 90°, it should be noted that a tunable plasmonic FRs can be realized by varying the width (D) of the CRA unit cells of the varied ϕ-shaped hybrid metasurface. Therein, the depth (width) of one of the Fano dips, located at the shorter wavelength side, first increases (decreases) then decreases (increases), while the depth (width) of the other Fano dip that locates at the longer wavelength side just increases (decreases) when D is changed from 15 to 35 nm. Moreover, the MICMT also agrees well with the numerical simulation by using Equation (5), as shown in the pink circles in Fig. 3(e), when the width D equals to 30 nm. The fitting parameters of this plasmonic DFRs can be given as follows: $N = 4$, $\omega_1 = 3.5328 \times 10^{14}$ rad/s, $\omega_2 = 3.2222 \times 10^{14}$ rad/s, $\omega_3 = 2.5514 \times 10^{14}$ rad/s, $\omega_4 = 1.7329 \times 10^{14}$ rad/s, $\tau_1 = 1700$ fs, $\tau_2 = 1550$ fs, $\tau_3 = 370$ fs, $\tau_4 = 255$ fs, $\tau_{10} = 1$ fs, $\tau_{20} = 75$ fs, $\tau_{30} = 165$ fs, $\tau_{40} = 225$ fs, $\varphi_1 = 0$, $\varphi_2 = -0.90$, $\varphi_3 = -0.11$ and $\varphi_4 = 0.32$. These results elucidate that, by adjusting the polarization angle of the incident light field and the width (D) of the CRA unit cells, the near-infrared plasmonic FR and DFRs with different physical mechanisms can be achieved in reduced ϕ-shaped, ϕ-shaped and varied ϕ-shaped hybrid metasurfaces, respectively. Simultaneously, we also show that the width and depth of the Fano dips, in varied ϕ-shaped and ϕ-shaped hybrid metasurfaces, can respectively be controlled by modulating the related geometric parameters of the unit cells, where the transmittance spectra significantly rely on the width of the CRA unit cells. The tailorable plasmonic DFRs may have broad practical applications in plasmonic sensing [22,57], plasmonic optical switches [23], and digital metasurface [40,58,59], as well as polarization-selective multispectral imaging applications [60], where the hybrid metasurfaces can be directly mounted on a charge-coupled-device camera [61].

3.3. Plasmonic sensing induced by single FR and DFRs

It is found that the resonance mode-broadening and mode-shifting sensing are self-referenced detection mechanisms. The mode-broadening sensing that has been proven to be particularly suitable for detecting lossy nanoparticle and monitoring the change of mode linewidth holds great potential in optical biosensing [1,37]. However, the mode-shifting sensing can be devoted to detecting changes in physical parameters surrounding the WGM resonators, such as pressure, heat, and magnetic fields [38,62]. Here, we focus on the polarization-sensitive resonance mode-broadening sensing and geometric-parameter-dependent mode-shifting sensing in the ϕ-shaped hybrid metasurface. When the polarization angle of the incident light is 0° (see the red curve in Fig. 4(a)), the transmittance spectrum exhibits a maximal peak at 1055 nm (peak-I) that represents the double bonding mode ($D_{\phi}^{z} + D_{\mathrm{CRA}}^{z}$), resulting from the Purcell effect caused by the WGM mode generated by the CRA unit cells [63]. When the polarization angle is changed from 0° to 90° in 10° step, the peak value of peak-I decreases gradually, with a minimum that it is in the context of 80° (see the blue curve in Fig. 4(a)). This is mainly due to the rectangular part of the ϕ-shaped structure is not explicitly activated, when the polarization direction of the incident light is nearly parallel to the ϕ-shaped-hole structure. When the polarization angle of incident light changes from 30° to 60°, it is important to note that the presence of peak-I reveals the plasmonic DFRs in the near-infrared waveband, which is the selectively excited triple bonding mode formed by the interaction between the double bonding ($D_{\phi}^{z} + D_{\mathrm{CRA}}^{z}$) and the double bonding ($D_{\phi}^{x} + D_{\mathrm{CRA}}^{x}$) modes. Moreover, when the polarization angle of the incident light is changed from 0° to 360° in 10° step, the transmittance spectra disclose different degrees of anisotropy, which also promise new capabilities for plasmonic sensing and switch, as shown in Fig. 4(b). Also, the full width at half maximum (FWHM) of the peak-I decreases exponentially as the polarization angle varies from 0° to 80°, as shown in Fig. 4(c). This phenomenon confirms that the exponential decay trend is a universal scaling behavior of the related plasmon coupling, and can be applied for achieving the high-sensitivity plasmonic sensing, which is independent of the shape and size of the nanostructure, the metal type, as well as the surrounding dielectric medium [64]. Furthermore, by adjusting the length (L) of ϕ-shaped-hole from 220 nm to 260 nm in 10 nm step, the geometric-parameter-dependent mode-shfiting plasmonic sensing can be realized in the ϕ-shaped hybrid metasurface, as shown in Fig. 4(d). In particular, the center wavelengths of peak-I and peak-II are redshift. It can be obviously seen that the transmittance of peak-I increases linearly (the red line in Fig. 4(d)), while that of the peak-II decreases exponentially (the green line in Fig. 4(d)). This behavior is conducive to monitoring and analysis of the biomolecular binding events [65,66]. Consequently, the polarization-sensitive resonance mode-broadening and geometric-parameter-dependent mode-shifting plasmonic sensing in the ϕ-shaped hybrid metasurface may have a wide range of applications in polarization cameras, biomedicine, and optical fiber communication.

3.4. Passive plasmonic switches and single-bit digital metasurface

It is noteworthy that the maximal and minimal of the transmittances can be established as the "ON" and "OFF" states of the plasmonic switch at the corresponding wavelengths, respectively. In our scheme, for the central wavelengths of 1055 nm and 1592 nm, their transmittance spectra can be controlled by adjusting the polarization direction of the incident light, as shown in Fig. 5(a). By shifting the orientation of the incident polarization may be possible to perform optical switch operation. The ON/OFF ratio (η) and modulation depth (MD) can be written as [67,68]:

$$\eta = 10\log_{10}\left(\frac{\mathcal{T}_{\mathrm{ON}}}{\mathcal{T}_{\mathrm{OFF}}}\right), \tag{6}$$

$$\mathrm{MD} = \left(1 - \frac{\mathcal{T}_{\mathrm{OFF}}}{\mathcal{T}_{\mathrm{ON}}}\right) \times 100\%, \tag{7}$$

where $\mathcal{T}_{\mathrm{ON}}$ and $\mathcal{T}_{\mathrm{OFF}}$ are the transmittances of "ON" and "OFF" states at the corresponding wavelength, respectively.

In Fig. 5(a), the "ON" and "OFF" states of the dual-wavelength passive plasmonic optical switches are displayed in the ϕ-shaped hybrid metasurface. For the case of the center wavelength at 1055 nm, the "ON" state of the plasmonic switch can be achieved with the transmittance being $\mathcal{T}_{\mathrm{ON}} = 0.5774$, when the polarization direction of the incident light (along the Z-direction) is perpendicular to the ϕ-shaped-hole unit cells. Whilst the "OFF" state of the plasmonic switch can be acquired with the transmittance being $\mathcal{T}_{\mathrm{OFF}} = 0.008268$, when the polarization direction of the incident light (along the X-direction) is parallel to the ϕ-shaped-hole unit cells. Thereby, the ON/OFF ratio (η) and the modulation depth (MD) of the central wavelength (1055 nm) can be obtained as 18.23 dB and 98.6% by using Equation (6) and Equation (7), respectively. For the case of the center wavelength at 1592 nm, which is located at the telecom L-band (1565~1625 nm), the transmittances of the "ON" and "OFF" states are $\mathcal{T}_{\mathrm{OFF}} = 0.009018$ and $\mathcal{T}_{\mathrm{ON}} = 0.8135$, respectively. Simultaneously, the ON/OFF ratio (η) of the center wavelength (1592 nm) can be obtained as 19.55 dB with the MD being 99%. These results indicate that a novel dual-wavelength passive plasmonic switches can be realized in the near-infrared region, which is a compact and passive device without adding another active pump light field in the hybrid metasurface. These polarization-sensitive dual-wavelength passive plasmonic switches, which contain high ON/OFF ratios, are advantageous to enhancing applications in optical communication with high flexibility and designability.

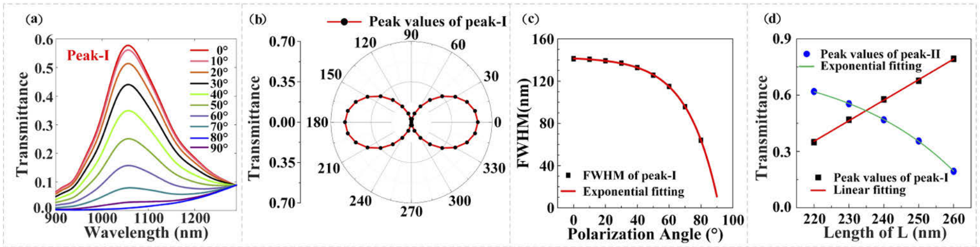

Fig. 4. The resonance mode-broadening and mode-shifting sensing in the ϕ-shaped hybrid metasurface. (a) The transmittance of the hybrid metasurface peaked at wavelength 1055 nm with different polarization angle of the incident light field. (b) Polar plots of the transmittance corresponding to peak-I. (c) The full width at half maximum (black square) and exponential fitting (red solid curve) of peak-I versus different polarization angle of the incident light field, respectively. (d) is the peak values of peak-I (black blocks) and peak-II (blue dots) with the length (L) of ϕ-shaped-hole increasing from 220 to 260 nm in 10 nm step, which are fitted by linear (red solid line) and exponential functions (green solid curve), respectively. The other parameters are the same as Fig. 2.

In order to further explore the physical mechanism of the plasmonic switches, we show the electric field distribution and the related polarization angles of the incident light of the ϕ-shaped hybrid metasurface in Fig. 5(b). With regard to the "ON" state of the plasmonic switch at 1055 nm, when the polarization direction of the incident light (0°, along the Z-direction) is perpendicular to the ϕ-shaped-hole unit cells, the strongest LSP resonance can be explicitly activated. This results from the presence of plasmonic FR, producing the double bonding mode ($D^z_\phi + D^z_{\mathrm{CRA}}$). The Purcell effect caused by the WGM mode generated by the CRA structure can further enhance the resonance intensity of ϕ-shaped-hole structure. However, with respect to the "OFF" state of the plasmonic switch at 1055 nm, when the polarization direction of the incident light (90°, along the X-direction) is parallel to the ϕ-shaped-hole unit cells, there is no obvious strong resonance occurring between the ϕ-shaped-hole and CRA unit cells in the ϕ-shaped hybrid metasurface. To the "ON" state of the plasmonic switch at 1592 nm, when the

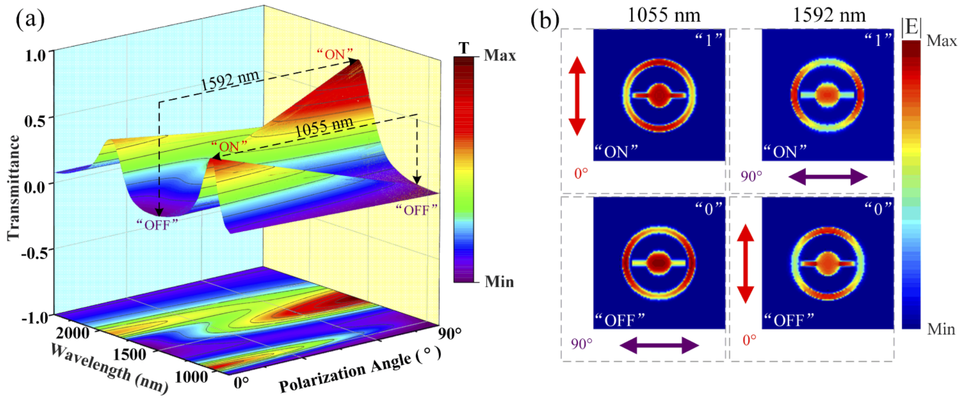

Fig. 5. Polarization-sensitive dual-wavelength passive plasmonic optical switches and single-bit digital metasurface. (a) The 3D surface-colormap surface with projection of passive plasmonic optical switches versus different wavelength and polarization angles of the incident light, with the high ON/OFF ratios being 18.23 dB and 19.55 dB for the center wavelengths at 1055 nm and 1592 nm, respectively. (b) The electric field distribution and the related polarization angles of the incident light of the ϕ-shaped hybrid metasurface at the central wavelength of 1055 and 1592 nm, respectively. Based on the characteristics of optical switches, the single-bit digital metasurface can be obtained with binary digital elements that the "OFF" and "ON" states are encoded as "0" and "1", respectively. The other parameters are the same as Fig. 2.

polarization direction of the incident light is along the X-direction, the strong resonance does not emerge between the ϕ-shaped-hole and CRA unit cells in the ϕ-shaped hybrid metasurface, but only leads to the appearance of plasmonic FR with the double bonding mode ($D_{\phi}^{x} + D_{\mathrm{CRA}}^{x}$). For the "OFF" state of the plasmonic switch at 1592 nm, when the polarization direction of the incident light is along the Z-direction, the strongest LSP resonance can also be successfully activated in the ϕ-shaped hybrid metasurface, rendering the PIT effect with a dip near 1592 nm [69,70]. These results encapsulate that once the "ON" state of one of the dual-wavelength plasmonic switches occurs, the "OFF" state can be achieved at another wavelength under the same conditions, and vice versa. Furthermore, it should be noted that, with specific geometry, the origin of this anisotropy-optical-switch phenomenon is the in-plane asymmetric structure of the ϕ-shaped unit cells in the ϕ-shaped hybrid metasurface [71].

In accordance with the characteristics of the plasmonic switches, a single-bit digital metasurface can be obtained by encoding the "OFF" and "ON" states as "0" and "1" elements, respectively. It should be noted that the linearly polarized resonance can be defined as digital bits only if the ON/OFF ratio and modulation depth are larger than 10 dB and 90%, respectively. The physical implementation of this binary digital elements requires different responses to obtain significant amplitude changes in the transmittance spectra. In this sense, we define the amplitude responses of the transmittance spectra for the elements as:

$$\mathcal{A}_{\mathrm{n}} = \frac{n}{Q}\left(\mathcal{T}_{\mathrm{ON}} - \mathcal{T}_{\mathrm{OFF}}\right), n = 0, 1, \cdots, Q, \tag{8}$$

where $Q = (2^{\mathcal{B}} - 1)$ with $\mathcal{B}$ being the number of bits. By using the Equation (8), the single-bit digital metasurface can be achieved with $\mathcal{B} = 1$ and $n = 0, 1$. This implies that the high ON/OFF ratios dual-wavelength plasmonic switches are possible to allow for two types of single-bit digital metasurface in the ϕ-shaped hybrid metasurface.

3.5. Two- and three-bit digital metasurface induced by plasmonic DFRs

For the sake of preferably exhibiting the digital metasurface induced by the plasmonic DFRs, we aim at the two- and three-bit digital metasurface on the basis of the ϕ-shaped hybrid metasurface, which operates at the telecom L-band (1565 ~ 1625 nm). It has been demonstrated that the polarization-sensitive single-bit digital metasurface can be extended to two-bit or more [40]. For the two-bit digital metasurface, it can be established at the telecom L-band with the center wavelength being 1592 nm. According to Equation (8), with $\mathcal{B} = 2$ and $n = 0, 1, 2, 3$, the amplitude responses of the transmittance spectra for the elements can be defined as “00”, “01”, “10”, and “11”, respectively. Simultaneously, the polarization angles of the incident light are set as $\theta = 0°$, 36°, 56°, and 90°, respectively. It is worth noting that, by varying the polarization angle of the incident light, the transmittance spectra change from plasmonic FR ($\theta = 0°$) to plasmonic DFRs ($\theta = 36°$and 56°), and then evolve in the absence of plasmonic FR ($\theta = 90°$).

In Fig. 6(a), the eight polarization angles of the incident light ($\theta = 0°, 21°, 31°, 40°, 48°, 56°, 66°$ and 90°) elicit different amplitude responses in the transmittance spectra for achieving a three-bit digital metasurface at 1592 nm. According to Equation (8), with $\mathcal{B} = 3$ and $n = 0, 1, 2, \cdots, 7$, we can define the amplitude responses of the transmittance spectra for the elements “000”, “001”, “010”, “011”, “100”, “101”, “110” and “111”, respectively. As shown in Fig. 6(a), when the polarization angle of incident light is 0° (21°), the amplitude response transmittance spectrum can be defined as “000” (“001”), see the red (yellow) curve in Fig. 6(a)). When the polarization angles are 31°, 40°, 48°, and 56°, the amplitude responses transmittance spectra (see the purple, black, green, and wine-red curves in Fig. 6(a)) can be set as “010”, “011”, “101”, and “110”, respectively. When the polarization angles are 66° and 90°, the amplitude responses transmittance spectra can be installed as “110” and “111” (see the orange and blue curves in Fig. 6(a)), respectively. As shown in Fig. 6(b), for the CRA unit cells of the hybrid metasurface, the orientations of the E-field distributions are coincide with the polarization directions of the corresponding incident light. However, for the ϕ-shaped unit cells of the hybrid metasurface, the orientations of the E-field distributions show that they are symmetric ($\theta = 0°$ and 90°), but are asymmetric ($\theta =$ 21°, 31°, 40°, 48°, 56°, and 66°) with respect to the axes (X- and Z-direction). This can be ascribed to the geometric configuration of the ϕ-shaped-hole unit cells being asymmetric along the polarization direction of the incident light. It is worth noting that, by varying the polarization angle of the incident light, the transmittance spectra change from plasmonic FR ($\theta = 0°$, 21°) to plasmonic DFRs ($\theta = 31°$, 40°, 48°, and 56°), and then develop in the absence of plasmonic FR ($\theta = 66°$, 90°). For this three-bit digital metasurface, the size of subwavelength nanostructures may be suitable for the integration and extension with the speed and high bandwidth of dielectric photonics, which also offer a much greater degree of flexibility in rapid data transmission and signal processing without adding complex control circuits. Thus, the proposed ϕ-shaped hybrid metasurface device can perform numerous functions and serves as a theoretical foundation for applications in optical sensing, optical digital processing, optical communication, and optical switches in the near-infrared waveband.

Besides, It is well known that the magnetron sputtered system seems to be an optimal platform allowing for the deposition of metals thin films onto a wide range of substrate [72]. In many situations, magnetron sputtering often outperform other techniques that is formed by conventional physical vapor deposition techniques, leading to the presence of high-quality metallic Ag film. In this way, first, magnetron sputtering is a widely used process for fabricating a thickness of 50 nm Ag film on a quartz substrate. For the quartz substrate, the silicon substrate was boiled (one hour at 393.15 K) in an $H_2SO_4 : H_2O_2$ composite solution (3:1), and then cleaned ultrasonically in acetone and deionized water, as well as dried with nitrogen. These processes result in the formation of a natural oxide layer that is the quartz substrate [73]. Second, a focused-ion beam technique can be used to produce extremely symmetrical nanoholes with diameters of sub-5 nm. After developing in a developer solution, the hybrid metasurface can be obtained

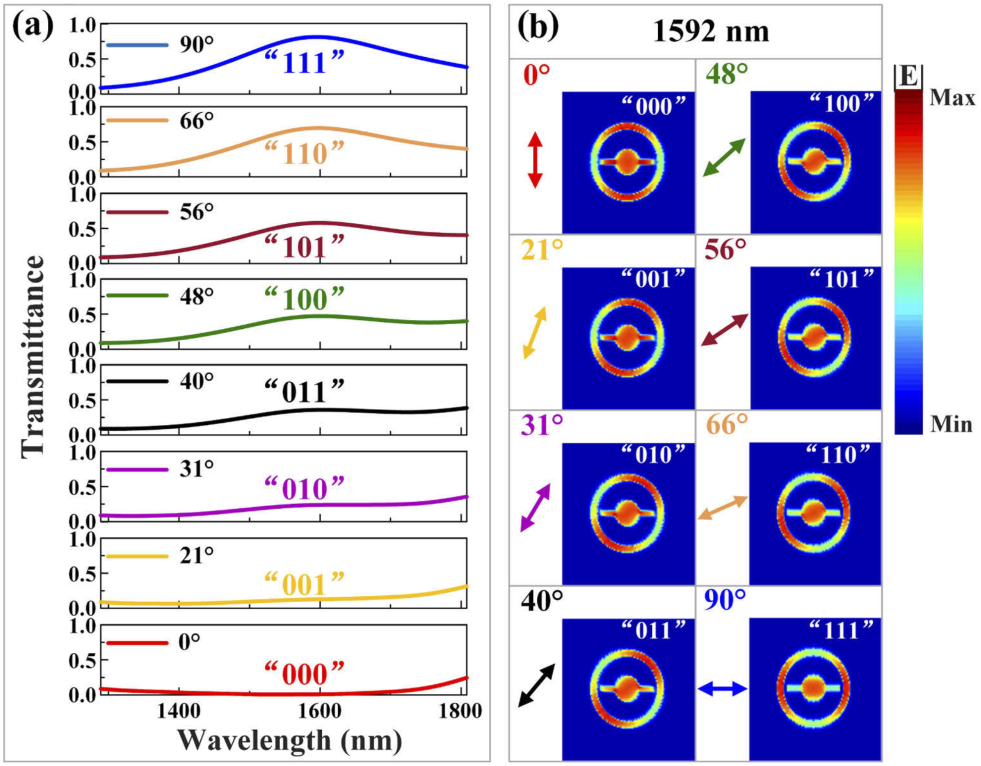

Fig. 6. The polarization-sensitive transmittance spectra for the three-bit digital metasurface at the center wavelength 1592 nm. (a) The amplitude responses of the three-bit digital metasurface by encoding the polarization-sensitive transmittance spectra with the polarization angle θ being 0°, 21°, 31°, 40°, 48°, 56°, 66° and 90°. (b) The "000", "001", "010", "011", "100", "101","110" and "111" coding elements are realized at 1592 nm. These eight subgraphs show the electric field distributions on the related polarization direction of the incident light. The other parameters are the same as Fig. 2.

with ϕ-shaped-hole and CRA unit cells [74]. For the measurement of the transmission spectra, the hybrid metasurface is illuminated with a modulated ultra-short Gaussian pulse, with the polarization direction of the incident light being modulating by the polarization controller. Finally, a homebuilt optical system can be used to collect the transmitted signal by a spectrometer with a charge-coupled device detector [75]. Herein, the Gaussian pulse can be focused on the hybrid metasurface by one of the near-infrared objective lenses, while the transmittance light is collected by the other near-infrared objective lens. Therefore, the proposed three different ϕ-shaped hybrid metasurfaces can be fabricated, and the plasmonic sensing and digital metasurface via DFRs can be observed in the experiment.

4. Conclusions

To sum up, we have studied the plasmonic DFRs for the realization of plasmonic sensing and digital metasurface in a novel hybrid metasurface that consists of periodic Ag film arrays with concentric ϕ-shaped-hole and CRA unit cells. It is shown that the near-infrared plasmonic FR, which originates from the interaction between the superradiant (D^z_{CRA}) and subradiant (D^z_{ϕ}) modes, can be realized. By adjusting the polarization angle of the incident light field and the width (D) of the CRA unit cells, we show that the near-infrared plasmonic DFRs with different physical mechanisms can be achieved in reduced-ϕ-shaped, ϕ-shaped, and varied-ϕ-shaped hybrid metasurfaces, respectively. In particular, the triple bonding and triple anti-bonding modes yielding from the plasmonic DFRs, which are well verified by the multimode interference coupled mode theory, can be illustrated in detail based on the plasmon hybridization theory under the polarization angle of the incident light being 45°. Therein, for the *reduced-ϕ-shaped hybrid metasurface*, the triple bonding (anti-bonding) mode originates from the interaction between the double bonding and double bonding (anti-bonding) modes with *selective excitation* (*degenerate coupling*). For the *ϕ-shaped hybrid metasurface*, the triple bonding mode stems from the interaction between double bonding and double bonding (anti-bonding) modes with (without) *selective excitation*, while the triple anti-bonding mode results from the interaction between the double bonding and double anti-bonding modes. For the *varied-ϕ-shaped hybrid metasurfaces*, the triple bonding mode arises from the interaction between the double bonding and double bonding modes, but the triple anti-bonding mode roots in the interaction between double anti-bonding (bonding) and double anti-bonding (bonding) modes with (without) *degenerate coupling*. The width and depth of the Fano dips of the plasmonic DFRs can be controlled by modulating the related geometric parameters of the unit cells in ϕ-shaped and varied ϕ-shaped hybrid metasurfaces, respectively. Subsequently, the polarization-sensitive resonance mode-broadening plasmonic sensing can be realized by varying the polarization direction of the incident light, whereas the geometric-parameter-dependent mode-shifting plasmonic sensing can be implemented by modifying the length (L) of ϕ-shaped-hole in the ϕ-shaped hybrid metasurface. Based on the maximal and minimal of the transmittances, the novel compact dual-wavelength passive plasmonic switches can be achieved with the ON/OFF ratios (η) being 18.23 dB and 19.55 dB, respectively. In doing so, the dual-wavelength plasmonic optical switches are beneficial to establish two types of single-bit digital metasurface whose "OFF" and "ON" states are encoded as "0" and "1", respectively. Furthermore, for the sake of preferably exhibiting the digital metasurface induced by the plasmonic DFRs, the two- and three-bit digital metasurface can be accomplished by encoding the four and eight different amplitude responses of the transmittance spectra as the elements at the telecom L-band, respectively. Our findings provide the fundamental basis for optical sensors, optical digital processing, modulators, and miniaturized wireless communication systems. More importantly, unlike the electronically controlled counterparts, this optically controlled hybrid metasurface can be extended to all-optical devices, which also holds great promise for broad applications.

Funding. Hunan Province Key Laboratory for Ultrafast Micro/Nano Technology and Advanced Laser Manufacture (2018TP1041); Foundation of Hunan Educational Committee (19C1585); Natural Science Foundation of Hunan Province (2020JJ5466); National Natural Science Foundation of China (12104214, 61835013, 62074091, U1930402); National Key Research and Development Program of China (2016YFA0301200, 2021YFA0718300, 2021YFA1400243, 2021YFA1400900); Science Challenge Project (TZ2018003).

Acknowledgments. X.-Q.L. and X.-L.W. acknowledge the support by the Hunan Province Key Laboratory for Ultrafast Micro/Nano Technology and Advanced Laser Manufacture (Grant No. 2018TP1041). X.-Q.L acknowledges the support by the Foundation of Hunan Educational Committee (Grant No. 19C1585), the Natural Science Foundation of Hunan Province of China (Grant No. 2020JJ5466), and the National Natural Science Foundation of China (Grants No. 12104214). T.-F.L acknowledges the support by the National Key Research and Development Program of China (Grant No. 2016YFA0301200), the National Natural Science Foundation of China (Grants No. 62074091 and No. U1930402), and Science Challenge Project (Grant No. TZ2018003). W.-M.L acknowledges the support by the National Key Research and Development Program of China (Grants No. 2021YFA1400900, No. 2021YFA0718300, and No. 2021YFA1400243), and the National Natural Science Foundation of China (Grants No. 61835013)..

Disclosures. The authors declare no conflicts of interest.

Data availability. Data underlying the results presented in this paper are not publicly available at this time but may be obtained from the authors upon reasonable request.

References

1. Y. Hu, L. Shao, S. Arnold, Y. C. Liu, C. Y. Ma, and Y. F. Xiao, "Mode broadening induced by nanoparticles in an optical whispering-gallery microcavity," Phys. Rev. A **90**(4), 043847 (2014).

2. B. Gerislioglu, L. Dong, A. Ahmadivand, H. Hu, P. Nordlander, and N. J. Halas, “Monolithic Metal Dimer-on-Film Structure: New Plasmonic Properties Introduced by the Underlying Metal,” Nano Lett. **20**(3), 2087–2093 (2020).
3. X. Li, Z.-Q. Dong, Y. Peng, L.-P. Wang, X.-D. Niu, H. Yamaguchi, and D.-C. Li, “Effect of self-assembly on fluorescence in magnetic multiphase flows and its application on the novel detection for COVID-19,” Phys. Fluids **33**(4), 042004 (2021).
4. J. Sun, H. Du, Z. Chen, L. Wang, and G. Shen, “MXene quantum dot within natural 3D watermelon peel matrix for biocompatible flexible sensing platform,” Nano Res., 1–7 (2021).
5. S. Q. Zhai, J. Q. Liu, F. Q. Liu, and Z. G. Wang, “A normal incident quantum cascade detector enhanced by surface plasmons,” Appl. Phys. Lett. **100**(18), 181104 (2012).
6. P. Wang, L. Wang, H. Leung, and G. Zhang, “Super-Resolution Mapping Based on Spatial–Spectral Correlation for Spectral Imagery,” IEEE Trans. Geosci. Remote Sens. **59**(3), 2256–2268 (2021).
7. J. Dostalek, J. Čtyroký, J. Homola, E. Brynda, M. Skalský, P. Nekvindova, J. Špirková, J. Škvor, and J. Schröfel, “Surface plasmon resonance biosensor based on integrated optical waveguide,” Sens. Actuators, B **76**(1-3), 8–12 (2001).
8. S. B. Glybovski, S. A. Tretyakov, P. A. Belov, Y. S. Kivshar, and C. R. Simovski, “Metasurfaces: From microwaves to visible,” Phys. Rep. **634**, 1–72 (2016).
9. H. T. Chen, A. J. Taylor, and N. Yu, “A review of metasurfaces: physics and applications,” Rep. Prog. Phys. **79**(7), 076401 (2016).
10. X. G. Zhang, W. X. Jiang, H. L. Jiang, Q. Wang, H. W. Tian, L. Bai, Z. J. Luo, S. Sun, Y. Luo, and C. W. Qiu, “An optically driven digital metasurface for programming electromagnetic functions,” Nat. Electron. **3**(3), 165–171 (2020).
11. B. Groever, W. T. Chen, and F. Capasso, “Meta-lens doublet in the visible region,” Nano Lett. **17**(8), 4902–4907 (2017).
12. X. Ni, S. Ishii, A. V. Kildishev, and V. M. Shalaev, “Ultra-thin, planar, babinet-inverted plasmonic metalenses,” Light: Sci. Appl. **2**(4), e72 (2013).
13. M. Wei, Q. Xu, Q. Wang, X. Zhang, Y. Li, J. Gu, Z. Tian, X. Zhang, J. Han, and W. Zhang, “Broadband non-polarizing terahertz beam splitters with variable split ratio,” Appl. Phys. Lett. **111**(7), 071101 (2017).
14. F. Ding, R. Deshpande, C. Meng, and S. I. Bozhevolnyi, “Metasurface-enabled broadband beam splitters integrated with quarter-wave plate functionality,” Nanoscale **12**(26), 14106–14111 (2020).
15. M. Khorasaninejad, W. Chen, A. Zhu, J. Oh, R. Devlin, D. Rousso, and F. Capasso, “Multispectral chiral imaging with a metalens,” Nano Lett. **16**(7), 4595–4600 (2016).
16. F. Cheng, J. Gao, T. S. Luk, and X. Yang, “Structural color printing based on plasmonic metasurfaces of perfect light absorption,” Sci. Rep. **5**(1), 11045 (2015).
17. B. Gerislioglu, G. Bakan, R. Ahuja, J. Adam, Y. K. Mishra, and A. Ahmadivand, “The role of $Ge_2Sb_2Te_5$ in enhancing the performance of functional plasmonic devices,” Mater. Today Phys. **12**, 100178 (2020).
18. U. Fano, “Effects of configuration interaction on intensities and phase shifts,” Phys. Rev. **124**(6), 1866–1878 (1961).
19. A. E. Miroshnichenko, S. Flach, and Y. S. Kivshar, “Fano resonances in nanoscale structures,” Rev. Mod. Phys. **82**(3), 2257–2298 (2010).
20. B. Luk’yanchuk, N. I. Zheludev, S. A. Maier, N. J. Halas, P. Nordlander, H. Giessen, and C. T. Chong, “The Fano resonance in plasmonic nanostructures and metamaterials,” Nat. Mater. **9**(9), 707–715 (2010).
21. W. Shang, F. Xiao, W. Zhu, H. He, M. Premaratne, T. Mei, and J. Zhao, “Fano resonance with high local field enhancement under azimuthally polarized excitation,” Sci. Rep. **7**(1), 1–8 (2017).
22. M. Mesch, B. Metzger, M. Hentschel, and H. Giessen, “Nonlinear plasmonic sensing,” Nano Lett. **16**(5), 3155–3159 (2016).
23. W. S. Chang, J. B. Lassiter, P. Swanglap, H. Sobhani, S. Khatua, P. Nordlander, N. J. Halas, and S. Link, “A plasmonic Fano switch,” Nano Lett. **12**(9), 4977–4982 (2012).
24. H. Xu, M. Zhao, C. Xiong, B. Zhang, M. Zheng, J. Zeng, H. Xia, and H. Li, “Dual plasmonically tunable slow light based on plasmon-induced transparency in planar graphene ribbon metamaterials,” Phys. Chem. Chem. Phys. **20**(40), 25959–25966 (2018).
25. Z. Li, W. Liu, Z. Li, H. Cheng, S. Chen, and J. Tian, “Fano-resonance-based mode-matching hybrid metasurface for enhanced second-harmonic generation,” Opt. Lett. **42**(16), 3117–3120 (2017).
26. Z. Chen, S. Zhang, Y. Chen, Y. Liu, P. Li, Z. Wang, X. Zhu, K. Bi, and H. Duan, “Double Fano resonances in hybrid disk/rod artificial plasmonic molecules based on dipole-quadrupole coupling,” Nanoscale **12**(17), 9776–9785 (2020).
27. N. Liu, M. Hentschel, T. Weiss, A. P. Alivisatos, and H. Giessen, “Three-dimensional plasmon rulers,” Science **332**(6036), 1407–1410 (2011).
28. D.-C. Wang, R. Tang, Z. Feng, S. Sun, S. Xiao, and W. Tan, “Symmetry-assisted spectral line shapes manipulation in dielectric double-Fano metasurfaces,” Adv. Opt. Mater. **9**(4), 2001874 (2021).
29. J. Wang, C. Fan, J. He, P. Ding, E. Liang, and Q. Xue, “Double Fano resonances due to interplay of electric and magnetic plasmon modes in planar plasmonic structure with high sensing sensitivity,” Opt. Express **21**(2), 2236–2244 (2013).
30. M. F. Limonov, “Fano resonance for applications,” Adv. Opt. Photonics **13**(3), 703–771 (2021).
31. V. Fedotov, M. Rose, S. Prosvirnin, N. Papasimakis, and N. Zheludev, “Sharp trapped-mode resonances in planar metamaterials with a broken structural symmetry,” Phys. Rev. Lett. **99**(14), 147401 (2007).

32. A. E. Miroshnichenko and Y. S. Kivshar, "Fano resonances in all-dielectric oligomers," Nano Lett. **12**(12), 6459–6463 (2012).
33. A. S. Shorokhov, E. V. Melik-Gaykazyan, D. A. Smirnova, B. Hopkins, K. E. Chong, D. Y. Choi, M. R. Shcherbakov, A. E. Miroshnichenko, D. N. Neshev, A. A. Fedyanin, and Y. S. Kivshar, "Multifold enhancement of third-harmonic generation in dielectric nanoparticles driven by magnetic Fano resonances," Nano Lett. **16**(8), 4857–4861 (2016).
34. S.-D. Liu, E. S. P. Leong, G.-C. Li, Y. Hou, J. Deng, J. H. Teng, H. C. Ong, and D. Y. Lei, "Polarization-independent multiple Fano resonances in plasmonic nonamers for multimode-matching enhanced multiband second-harmonic generation," ACS Nano **10**(1), 1442–1453 (2016).
35. N. Liu, S. Mukherjee, K. Bao, L. V. Brown, J. Dorfmüller, P. Nordlander, and N. J. Halas, "Magnetic plasmon formation and propagation in artificial aromatic molecules," Nano Lett. **12**(1), 364–369 (2012).
36. M. Xiong, X. Jin, and J. Ye, "Strong plasmon coupling in self-assembled superparamagnetic nanoshell chains," Nanoscale **8**(9), 4991–4999 (2016).
37. B. Q. Shen, X. C. Yu, Y. Zhi, L. Wang, D. Kim, Q. Gong, and Y. F. Xiao, "Detection of single nanoparticles using the dissipative interaction in a high-Q microcavity," Phys. Rev. Appl. **5**(2), 024011 (2016).
38. M. R. Foreman, J. D. Swaim, and F. Vollmer, "Whispering gallery mode sensors," Adv. Opt. Photonics **7**(2), 168 (2015).
39. A. Overvig and A. Alú, "Wavefront-selective Fano resonant metasurfaces," Adv. Photonics **3**(2), 026002 (2021).
40. J. Ou, X. Q. Luo, Y. L. Luo, W. H. Zhu, Z. Y. Chen, W. M. Liu, and X. L. Wang, "Near-infrared dual-wavelength plasmonic switching and digital metasurface unveiled by plasmonic Fano resonance," Nanophotonics **10**(2), 947–957 (2020).
41. M. Besbes, J. P. Hugonin, P. Lalanne, S. van Haver, O. T. A. Janssen, A. M. Nugrowati, M. Xu, S. F. Pereira, H. P. Urbach, A. S. van de Nes, P. Bienstman, G. Granet, A. Moreau, S. Helfert, M. Sukharev, T. Seideman, F. I. Baida, B. Guizal, and D. V. Labeke, "Numerical analysis of a slit-groove diffraction problem," J. Europ. Opt. Soc. Rap. Public. **2**, 07022 (2007).
42. Y. Xu, L. Chen, X. Wang, W. Yao, and Q. Zhang, "Recent advances in noble metal based composite nanocatalysts: colloidal synthesis, properties, and catalytic applications," Nanoscale **7**(24), 10559–10583 (2015).
43. J. M. McMahon, J. Henzie, T. W. Odom, G. C. Schatz, and S. K. Gray, "Tailoring the sensing capabilities of nanohole arrays in gold films with Rayleigh anomaly-surface plasmon polaritons," Opt. Express **15**(26), 18119–18129 (2007).
44. F. Zhen, Z. Chen, and J. Zhang, "Toward the development of a three-dimensional unconditionally stable finite-difference time-domain method," IEEE Trans. Microwave Theory Technol. **48**(9), 1550–1558 (2000).
45. T. Wang and G. W. Hohmann, "A finite-difference, time-domain solution for three-dimensional electromagnetic modeling," Geophysics **58**(6), 797–809 (1993).
46. W. Chew and Q. Liu, "Perfectly matched layers for elastodynamics: a new absorbing boundary condition," J. Comp. Acous. **4**(04), 341–359 (1996).
47. J. Chen, J. Li, X. Liu, S. Rohimah, H. Tian, and D. Qi, "Fano resonance in a mim waveguide with double symmetric rectangular stubs and its sensing characteristics," Opt. Commun. **482**, 126563 (2021).
48. S. Zhang, K. Bao, N. J. Halas, H. Xu, and P. Nordlander, "Substrate-induced Fano resonances of a plasmonic nanocube: A route to increased-sensitivity localized surface plasmon resonance sensors revealed," Nano Lett. **11**(4), 1657–1663 (2011).
49. A. Muravitskaya, A. Gokarna, A. Movsesyan, S. Kostcheev, A. Rumyantseva, C. Couteau, G. Lerondel, A. L. Baudrion, S. Gaponenko, and P. M. Adam, "Refractive index mediated plasmon hybridization in an array of aluminium nanoparticles," Nanoscale **12**(11), 6394–6402 (2020).
50. D. Gómez, Z. Q. Teo, M. Altissimo, T. J. Davis, S. Earl, and A. Roberts, "The dark side of plasmonics," Nano Lett. **13**(8), 3722–3728 (2013).
51. Y. Sonnefraud, N. Verellen, H. Sobhani, G. A. Vandenbosch, V. V. Moshchalkov, P. Van Dorpe, P. Nordlander, and S. A. Maier, "Experimental realization of subradiant, superradiant, and fano resonances in Ring/Disk plasmonic nanocavities," ACS. Nano. **4**(3), 1664–1670 (2010).
52. S. Li, Y. Wang, R. Jiao, L. Wang, G. Duan, and L. Yu, "Fano resonances based on multimode and degenerate mode interference in plasmonic resonator system," Opt. Express **25**(4), 3525–3533 (2017).
53. J. Chen, K. He, C. Sun, Y. Wang, H. Li, and Q. Gong, "Tuning Fano resonances with a nano-chamber of air," Opt. Lett. **41**(10), 2145–2148 (2016).
54. J. R. Piper, V. Liu, and S. Fan, "Total absorption by degenerate critical coupling," Appl. Phys. Lett. **104**(25), 251110 (2014).
55. X. Ming, X. Liu, L. Sun, and W. J. Padilla, "Degenerate critical coupling in all-dielectric metasurface absorbers," Opt. Express **25**(20), 24658–24669 (2017).
56. Y. Park, J. Kim, Y. G. Roh, and Q. H. Park, "Optical slot antennas and their applications to photonic devices," Nanophotonics **7**(10), 1617–1636 (2018).
57. B. Špačková, P. Wrobel, M. Bocková, and J. Homola, "Optical biosensors based on plasmonic nanostructures: a review," Proc. IEEE **104**(12), 2380–2408 (2016).
58. T. J. Cui, M. Q. Qi, X. Wan, J. Zhao, and Q. Cheng, "Coding metamaterials, digital metamaterials and programmable metamaterials," Light: Sci. Appl. **3**(10), e218 (2014).

59. J. Li, Y. Zhang, J. Li, X. Yan, L. Liang, Z. Zhang, J. Huang, J. Li, Y. Yang, and J. Yao, "Amplitude modulation of anomalously reflected terahertz beams using all-optical active Pancharatnam–Berry coding metasurfaces," Nanoscale **11**(12), 5746–5753 (2019).
60. G. ElMasry, N. Mandour, S. Al-Rejaie, E. Belin, and D. Rousseau, "Recent applications of multispectral imaging in seed phenotyping and quality monitoring–an overview," Sensors **19**(5), 1090 (2019).
61. X. Zang, F. Dong, F. Yue, C. Zhang, L. Xu, Z. Song, M. Chen, P. Y. Chen, G. S. Buller, Y. Zhu, S. Zhuang, W. Chu, S. Zhang, and X. Chen, "Polarization encoded color image embedded in a dielectric metasurface," Adv. Mater. **30**(21), 1707499 (2018).
62. X. Jiang, A. J. Qavi, S. H. Huang, and L. Yang, "Whispering-gallery sensors," Matter **3**(2), 371–392 (2020).
63. E. J. R. Vesseur, F. J. G. de Abajo, and A. Polman, "Broadband purcell enhancement in plasmonic ring cavities," Phys. Rev. B **82**(16), 165419 (2010).
64. P. K. Jain and M. A. El-Sayed, "Universal scaling of plasmon coupling in metal nanostructures: extension from particle pairs to nanoshells," Nano Lett. **7**(9), 2854–2858 (2007).
65. Y. Zhang, Y. R. Zhen, O. Neumann, J. K. Day, P. Nordlander, and N. J. Halas, "Coherent anti-Stokes Raman scattering with single-molecule sensitivity using a plasmonic Fano resonance," Nat. Commun. **5**(1), 4424 (2014).
66. Y. Luo, X. Q. Luo, J. Yi, J. Ou, W. Zhu, Z. Chen, W. Liu, and X. Wang, "Whispering-gallery mode resonance-assisted plasmonic sensing and switching in subwavelength nanostructures," J. Mater. Sci. **56**(7), 4716–4726 (2021).
67. F. Chen and D. Yao, "Tunable multiple all-optical switch based on multi-nanoresonator-coupled waveguide systems containing kerr material," Opt. Commun. **312**, 143–147 (2014).
68. A. Ahmadivand, B. Gerislioglu, R. Sinha, M. Karabiyik, and N. Pala, "Optical switching using transition from dipolar to charge transfer plasmon modes in $Ge_2Sb_2Te_5$ bridged metallodielectric dimers," Sci. Rep. **7**(1), 42807 (2017).
69. K. J. Boller, A. Imamoglu, and S. E. Harris, "Observation of electromagnetically induced transparency," Phys. Rev. Lett. **66**(20), 2593–2596 (1991).
70. S. Zhang, D. A. Genov, Y. Wang, M. Liu, and X. Zhang, "Plasmon-induced transparency in metamaterials," Phys. Rev. Lett. **101**(4), 047401 (2008).
71. C. Zhang, H. Ouyang, R. Miao, Y. Sui, H. Hao, Y. Tang, J. You, X. Zheng, Z. Xu, X. Cheng, and T. Jiang, "Anisotropic nonlinear optical properties of a SnSe flake and a novel perspective for the application of all-optical switching," Adv. Opt. Mater. **7**(18), 1900631 (2019).
72. G. Bruer, B. Szyszka, M. Verghl, and R. Bandorf, "Magnetron sputtering–milestones of 30 years," Vacuum **84**(12), 1354–1359 (2010).
73. G. F. Liang, J. Jiao, X. G. Luo, and Q. Zhao, "Measurement and analysis of the surface roughness of ag film used in plasmonic lithography," Chin. Phys. B **26**(1), 016801 (2017).
74. C. J. Lo, T. Aref, and A. Bezryadin, "Fabrication of symmetric sub-5 nm nanopores using focused ion and electron beams," Nanotechnology **17**(13), 3264–3267 (2006).
75. Z. Liu, Y. Xu, C. Ji, S. Chen, X. Li, X. Zhang, Y. Yao, and J. Li, "Fano-enhanced circular dichroism in deformable stereo metasurfaces," Adv. Mater. **32**(8), 1907077 (2020).